Enhanced Photovoltaic Performance and Thermal Stability of $CH_3NH_3PbI_3$ Perovskite through Lattice Symmetrization

Feng Shao[a,b], Peng Qin[a,*], Dong Wang[a], Guoqing Zhang[a], Bo Wu[c], Jianqiao He[a], Wei Peng[d], Tze Chien Sum[c], Deliang Wang[b,*], and Fuqiang Huang[a,e,*]

[a] State Key Laboratory of High Performance Ceramics and Superfine Microstructure, Shanghai Institute of Ceramics, Chinese Academy of Sciences, Shanghai 200050, China.

[b] Hefei National Laboratory for Physical Sciences at the Microscale, University of Science and Technology of China, Hefei 230026, China.

[c] Division of Physics and Applied Physics, School of Physical and Mathematical Sciences, Nanyang Technological University, 21 Nanyang Link, Singapore 637371.

[d] State Key Laboratory of Functional Materials for Informatics, Shanghai Institute of Microsystem and Information Technology, Chinese Academy of Sciences, Shanghai 200050, China.

[e] State Key Laboratory of Rare Earth Materials Chemistry and Applications, College of Chemistry and Molecular Engineering, Peking University, Beijing 100871, China.

[*]Corresponding authors.

E-mail addresses: qinpeng@mail.sic.ac.cn (P. Qin), eedewang@ustc.edu.cn (D. Wang), huangfq@mail.sic.ac.cn (F. Huang).

Keywords: dimethyl ammonium, lattice symmetrization, charge extraction, perovskite solar cell, thermal stability

ABSTRACT

The organic−inorganic lead halide perovskites are attractive materials for photovoltaic application. The most widely studied perovskites based on methyl ammonium organic cation are less likely to form an ideal high-symmetry configuration at room temperature, leading to the appearance of local lattice strain. Herein, this study reports a strategy for the construction of thermally stable cubic perovskites at room temperature through the incorporation of the larger organic cation dimethyl ammonium. Detailed characterization on the single crystals and thin films reveals the formation of cubic phase with the addition of a certain amount of dimethyl ammonium at room temperature. With the presence of dimethyl ammonium, the nonradiative recombination in perovskite is suppressed, showing a longer PL lifetime and hole diffusion length. The more efficient charge extraction leads to an improvement in the photocurrent density, and then the device efficiency from 17.1% to 18.6%, together with an enhanced thermal stability at 85 °C. The influence of incorporating a larger organic cation on the structural configuration, optical properties, charge extraction, as well as the photovoltaic performance is systematically investigated, which offers an alternative way to improve the intrinsic stability of hybrid perovskites.

1. Introduction

Organic-inorganic lead halides ($APbX_3$) have been intensively investigated as light harvesters in the photovoltaic devices [1-4], light-emitting diodes [5-6], photodetectors etc [7-8], due to the high optical absorption coefficients, ambipolar carrier transport properties, long carrier diffusion lengths, high defect tolerance, and low-cost coating techniques [9-13]. Various optimization on crystal growth, fabrication techniques, as well as device configuration has allowed for a dramatic increase of device performance from 3.8% to over 22% in the past few years, rivalling the traditional thin film photovoltaics [14-25]. Besides the improvement of efficiency, the stability is another important issue for organic-inorganic perovskites considering their further applications. The widely studied methyl ammonium lead iodide ($MAPbI_3$) adopts the tetragonal configuration at room temperature, which is sensitive and prone to decompose under humidity, heat and light [26-27].

The symmerty of $MAPbI_3$ can be influenced by the lattice distortion or expansion throuth ion incorporating, temperature-induced phase transition or light illumination [28-33]. The formation of a cubic phase is expected to improve the thermal stability of perovskites, as well as suppress the nonradiative recombination for efficient charge extraction. It was found that the presence of FA^+ in $MAPbI_3$ stabilizes the perovskite structure into a "quasi-cubic" phase, which further limits light/field induced ion movement and impedes halide segregation [34]. Partial incorporation of ethyl ammonium (EA^+) cation leads to a cubic phase at room temperature, with enhanced thermal stability and charge carrier lifetime [35]. Mi and co-workers hypothesized that perovskites with ideal cubic structure would feature superior semiconductor properties and better stability [36]. They used the volume per

formula unit (*V*/*Z*) as an input parameter to model the mixed cation perovskites, and confirmed that the introduction of bigger cation could tune the $MAPbI_3$ toward the ideal limit with a higher crystal symmetry. The prepared cubic perovskites showhigher stability under 80% relative humidity with degradation lifetimes about ten times longer than that of $MAPbI_3$. Both theoretical and experimental studies offer the potential to build a more stable cubic configuration of perovskites by modification of the organic cation.

Herein, we report the growth of high-quality single crystals of $MA_{1-x}DMA_xPbI_3$ (x = 0 to 0.25) where MA^+ is gradually replaced by dimethyl ammonium DMA^+, and investigate the thermodynamic effects of MA^+/DMA^+ incorporation on structural configuration. The DMA^+ is inserted into the voids of the $[PbI_6]$ octahedra, tuning the perovskite structure into a more stable cubic phase at room temperature. The $MA_{1-x}DMA_xPbI_3$ perovskite solar cells with an optimized 5% DMA^+ doping (in terms of the molar ratio in the precursor solution) exhibit an improvement in device efficiency from 17.1% to 18.6%, together with an enhanced thermal stability at 85°C.

2. Experimental section

2.1. Growth of $MA_{1-x}DMA_xPbI_3$ (x = 0 to 0.25)single crystals.

The perovskite precursors with different molar ratio of MA^+/DMA^+ were dissolved in gamma-butyrolactone (GBL, 1.23 M) in a N_2 filled glove box. 0%, 1.0%, 2.5%, 5%, 10% and 20% of DMAI were tested. Small crystals with the size of 2-3 mm were obtained after heating the precursor solution at 95°C for 24 h. For large crystal growth, the small crystal was picked up and put again into a fresh perovskite precursor solution.

2.2. Solar Cell Fabrication

The etched fluorine-doped tin oxide (FTO) was cleaned with 2% Hellmanex aqueous solution, acetone, and ethanol, which was subsequently treated with O_2 plasma for 15 min. The compact TiO_2 layer (around 45 nm) was deposited on the top by spray pyrolysis from a precursor solution of titanium diisopropoxide bis (acetylacetonate) at 450 °C using O_2 as the carrier gas, followed by annealing at 450 °C for 30 min in air. The mesoporous TiO_2 film was deposited by spin-coating the diluted Dyesol 30NRD paste at 4000 rpm for 20 s, and then sintered at 500 °C for 30 min. The perovskite precursor solutions with different MA^+/DMA^+ ratio were prepared in a glove box including 1.6 M of PbI_2 and 1.52 M MAI/DMAI in anhydrous DMSO. 0%, 2.5%, 5%, 7.5%, and 10% molar ratio of DMAI were tested, which were labeled as $MA_{1-x}DMA_xPbI_3$ with x = 0, 0.025, 0.05, 0.075, and 0.10. The precursor solution was spin-coated in a two-step procedure at 1000 and 7000 rpm for 10 and 35 s, respectively. 120 μL of 3α-trifluorotoluene was dropped on the spinning substrate 15 s before the end of the second step. The substrate was then annealed at 100 °C for 1 h. After cooling down, the HTM solution of 0.06 M 2,2′,7,7′-tetrakis(N,N-di-p-methoxyphenylamine)-9,9′-spirobifluorene (spiro-MeOTAD), 0.03 M lithiumbis(trifluoromethylsulphonyl)imide (LiTFSI), 0.2 M 4-tert-butylpyridine (TBP), and 6×10^{-3} M of tris(2-(1H-pyrazol-1-yl) -4-tert-butylpyridine-cobalt(III)tris(bis(trifluoromethylsulfonyl)imide) (KF209) in chlorobenzene, was spin-coated on the top of the perovskite layer with a spin speed of 4000 rpm. Finally, 80 nm of Au was deposited by thermal evaporation under a pressure of 1×10^{-4} Torr as the back contact.

2.3. Photovoltaic Characterization

The current-voltage characteristics were measured using a 1000 W xenon light source (Newport). The light intensity was calibrated with a NREL-calibrated Si cell (Oriel 91150). The *J-V* curves of the devices were obtained by applying an external potential bias while measuring the responded photocurrent with a digital source meter (Keithley 2400) with a scan rate was 10 mV s^{-1}. The devices were measured by using a black mask with an active area of 0.16 cm^2. The IPCE spectra were measured using a 300 W xenon light source (Newport). For stability tests, the unsealed solar cells were kept in an ambient atmosphere (humidity > 50%) at 85°C, and the *J-V* curves were measured every 24 h.

3. Results and discussion

The single crystals of $MA_{1-x}DMA_xPbI_3$ (x = 0 to 0.25) were prepared by dissolving certain amount of PbI_2, MAI, and DMAI into a GBL solution [37]. Small black crystals, with the diameter of 2-3 mm, were obtained by keeping the precursor solutions onto a hotplate at 95°C for 24 h. The carbon, nitrogen and hydrogen elemental analysis was performed to determine the molar ratio of MA^+ and DMA^+ in the prepared crystals. As the reference, the mass fractions of $MAPbI_3$ were measured to be 2.00%, 2.29%, and 0.98% for C, N, and H, respectively, consistent with the theoretical calculation. With the addition of DMAI in the precursor solution, the molar proportion of DMA^+ was adjusted from 4% to 25%, which was 3-5% higher than that of the precursor solution in all the cases (Table S1).

In such kind of complex, the organic cations reside in the voids of $[PbI_6]$ octahedra. The ionic radii of the organic cations will influence the connection mode of neighboring corner-shared $[PbI_6]$ octahedra, and then the crystal configuration. Fig. 1a

shows the Powder X-ray diffraction (PXRD) patterns of the prepared $MA_{1-x}DMA_xPbI_3$ (x = 0 to 0.25) perovskites with increased DMA^+ concentration. $MAPbI_3$ with a distorted three-dimensional structure crystallizes in the tetragonal *I*4/*mcm* space group, which shows the peaks at 14.0°, 14.1°, 23.5°, 24.5°, 28.1°, and 28.4° indexing to the (002), (110), (211), (202), (004), and (220) lattice planes. With the addition of DMA^+, the organic cations MA^+ and DMA^+ are co-intercalated in the voids of $[PbI_6]$ octahedra. The organic cations interact with the inorganic framework through the dispersion interaction between the methyl and iodide ions. Due to the relatively weak van der Waals force, such bonding is possibly destroyed by the addition of one more methyl group. As shown in our experiments, the complex preserves the tetragonal structure when the amount of DMA^+ is less than 6%, showing clear split of the facets (002)/(110), (004)/(220), and the appearance of both (211) and (202). With further addition of DMA^+ at room temperature, these facets are gradually merged into single peaks due to the increased symmetry, indicating the formation of a more stable cubic phase (Fig. 1b). Moreover, with gradual substitution of large DMA^+, the systematic shift of the peaks toward lower 2θ is observed due to the increased lattice spacing, which leads to the expansion of the cell volume. The lattice parameters of as-prepared samples were matched, indexed, and refined using Jade 6.5, and the variations of lattice parameters were listed in Table 1. The *V*/*Z* of $MAPbI_3$ was calculated to be 248.98 $Å^3$, which boosts to 250.4 $Å^3$ as soon as the phase transition from tetragonal to cubic occurs with the addition of DMA^+. With further addition of DMA^+ up to 25%, the *V*/*Z* was calculated to be 254.8 $Å^3$, approaching the

maximum value (255 $Å^3$) that a closed PbI_3^- framework with a fixed *d*(Pd-I) and flexible ∠Pd-I-Pd can occupy [35]. To investigate the change of the optical properties of $MA_{1-x}DMA_xPbI_3$ (x = 0 to 0.25) perovskites as a function of DMA^+ content, the solid state reflection UV-vis spectra were measured (Fig. 1c). A band gap of 1.55 eV was extracted for $MAPbI_3$ from the Tauc plot, which undergoes negligible change when the substitution of DMA^+ gradually increases to 13%. Further addition of DMA^+ up to 25% leads to a lower band gap of 1.58 eV.

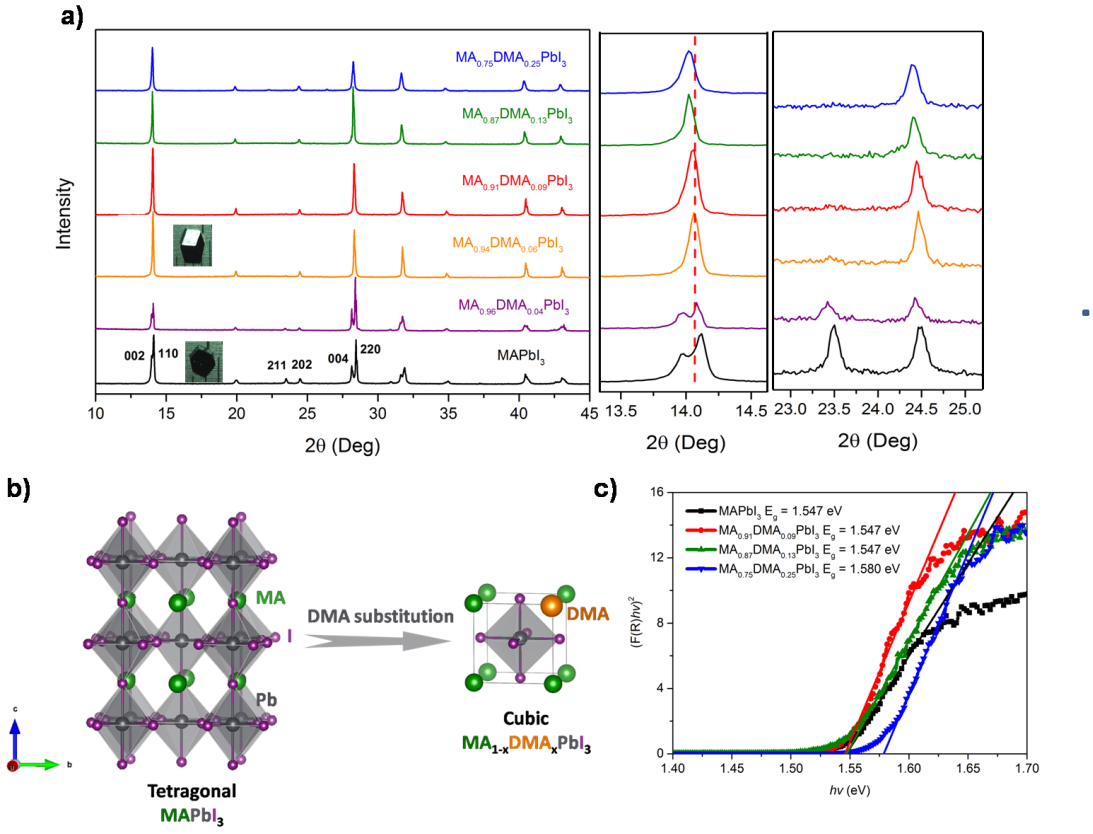

Fig. 1. (a) X-ray diffraction spectra of $MA_{1-x}DMA_xPbI_3$ (x = 0 to 0.25). (b) The schematic structure transformation patterns from tetragonal $MAPbI_3$ to cubic $MA_{1-x}DMA_xPbI_3$ (the green, orange, purple, and grey spheres represent MA, DMA, I, and Pb). (c) Tauc Plot of those with x = 0, 0.09, 0.13, and 0.25.

Table 1. The detailed cell parameters of the as-prepared $MA_{1-x}DMA_xPbI_3$ samples.

	Crystal system	*a* (Å)[a]	*c* (Å)[b]	*V* (Å^3)[c]	*Z* [d]	*V*/*Z* (Å^3)
$MAPbI_3$	Tetragonal	8.886	12.671	995.9	4	248.98
$MA_{0.96}DMA_{0.04}PbI_3$	Tetragonal	8.888	12.675	1001.2	4	250.30
$MA_{0.94}DMA_{0.06}PbI_3$	Quasi cubic	6.302	-	250.2	1	250.20
$MA_{0.91}DMA_{0.09}PbI_3$	Cubic	6.303	-	250.4	1	250.40
$MA_{0.87}DMA_{0.13}PbI_3$	Cubic	6.311	-	251.4	1	251.40
$MA_{0.75}DMA_{0.25}PbI_3$	Cubic	6.313	-	251.8	1	254.80

[a] *a* axial length; [b] *c* axial length; [c] unit cell volume; [d] the numbers of formula weight in one unit cell.

In order to determine the crystal structure of the cubic phase, $MA_{0.91}DMA_{0.09}PbI_3$, which was crystallized from the precursor solution with the MA^+/DMA^+ ratio of 0.95/0.05, was chosen as an example for further investigation. Single crystal X-ray diffraction results indicate that $MA_{0.91}DMA_{0.09}PbI_3$ crystallizes in the cubic *P*-43*m* space group (*a* = 6.303 Å) (Table S2). The bond length of Pb-I is 3.1515 Å, which is smaller than that of $MAPbI_3$ (3.1736 Å) due to the less distorted configuration of $[PbI_6]$ octahedra. In cubic $MA_{0.91}DMA_{0.09}PbI_3$, the bond angle of Pb-I-Pb is 180^o. Each Pb atom is surrounded by six face centred I atoms, forming regular $[PbI_6]$ octahedron, and two adjacent $[PbI_6]$ octahedra were connected to each other by corner-sharing. The corporate organic cations MA^+/DMA^+ were inserted in the voids of $[PbI_6]$ framework. As shown from the powder XRD pattern (Fig. S1), the red curve

represents the experimental data for $MA_{0.91}DMA_{0.09}PbI_3$, and the black one for the simulated counterpart derived from the single crystal results. All the diffraction peaks from the experimental data matchwell with the simulated lattice planes, indicating the high purity of $MA_{0.91}DMA_{0.09}PbI_3$.

Variable temperature powder X-ray diffractions were collected at 20°C intervals between -80°C to 80°C to monitor the in situ transformation for investigating the phase transition of $MA_{0.91}DMA_{0.09}PbI_3$ in more details. As shown from the diffraction patterns in tetragonal and cubic symmetry in Fig. 1a, the change in symmetry could be detected by monitoring the reflection at 23.5^o (2θ), accompanied by the splitting of (001) and (002) with higher intensities [27]. $MA_{0.91}DMA_{0.09}PbI_3$ keeps the cubic phase above 0°C. As soon as lower than 0°C, there is a clear appearance of (211) reflection at 23.5^o, which gradually increases toward lower temperature, indicating a cubic-tetragonal phase transition (Fig. 2 and S2). The lower cubic to tetragonal phase transition temperature of perovskite with the presence of DMA^+ cation is expected to possess better intrinsic thermal stability by avoiding the undesired lattice strain and distortion. With further decrease of the temperature to - 40°C, $MA_{0.91}DMA_{0.09}PbI_3$ undergoes a tetragonal to orthorhombic phase transition (Fig. 2 and S3) [38].

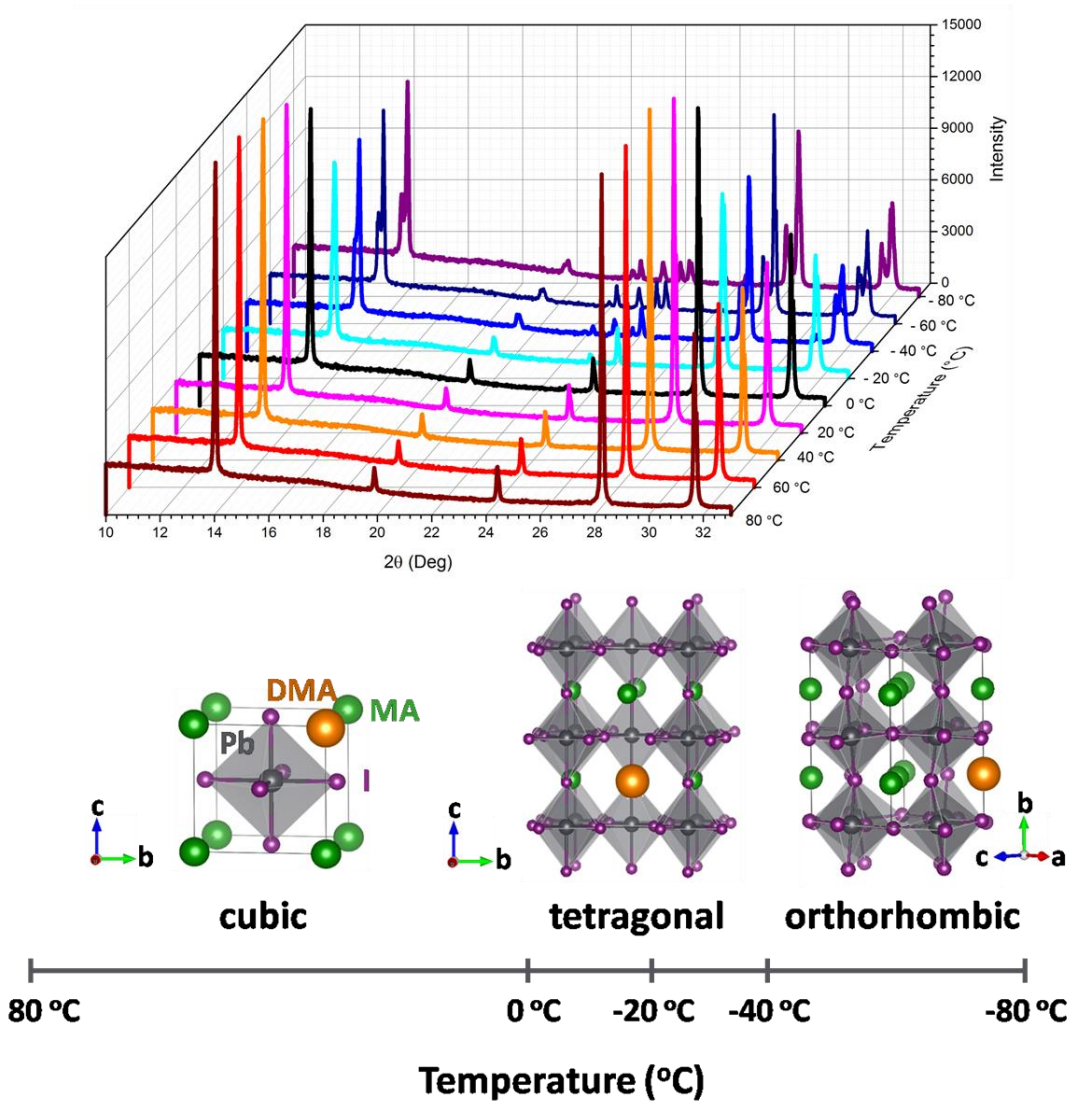

Fig. 2. The temperature-dependent XRD spectra (-80 to 80°C) and the corresponding schematic structure transformation patterns of $MA_{0.91}DMA_{0.09}PbI_3$.

The perovskite precursor solution was deposited directly on the mesoporous TiO_2 film to evaluate the effect of DMA^+ doping on the device performance. It was shown that high efficiency $MAPbI_3$ solar cells could be prepared by incorporating excess PbI_2 as an additive in the film, which improves the crystallinity of perovskite and the electron transfer to TiO_2 [39,40]. Therefore, all perovskite films in our study were prepared from the precursor solution with 5% molar excess of PbI_2. The films with pure $MAPbI_3$ solution and those with x = 0.05 were chosen for comparison. Fig. S4

show the SEM images obtained from the top surface of TiO_2/perovskite films. With the presence of DMA^+, the crystals are tightly arranged, showing a smoother surface with less pin-holes. As seen in Fig. 3a, there is almost no difference on the UV-vis absorption spectra of the two films, consistent with that measured on single crystals. The X-ray patterns confirm the presence of tetragonal perovskite phase in $MAPbI_3$ film. The unreacted PbI_2 peak located at 2θ of 12.7° is found in all the cases. With the presence of 5% DMA^+, the (211) reflection at 23.5° vanishes. Comparing with the earlier studies on crystals, the disappearance of the (211) reflection, together with a shift of the peaks toward lower 2θ indicate a phase transition from tetragonal to cubic (Fig. 3b).

The photoluminescence (PL) spectra of $MA_{1-x}DMA_xPbI_3$ (x = 0 and 0.05) deposited without (Al_2O_3/perovskite) and with (TiO_2/perovskite/spiro-MeOTAD) charge transporting materials are shown in Fig. 3c. Without the charge transporting materials, the PL intensity is much higher for the cubic $MA_{1-x}DMA_xPbI_3$ (x = 0.05) compared to $MAPbI_3$ (x= 0), indicating the suppression of nonradiative recombination. With the presence of charge transporting materials, both samples show a dramatic PL quenching with respect to the pristine perovskite, which is attributed to the efficient charge transfer at the TiO_2/perovskite and perovskite/spiro-MeOTAD interfaces. The time-resolved photoluminescence (TRPL) was performed to estimate the charge diffusion properties (Figure 3d). From the TRPL kinetics of the $MA_{1-x}DMA_xPbI_3$ (x = 0 and 0.05) films on quartz substrate, an increased PL lifetime from 44.0 ± 1.3 ns for $MAPbI_3$ pristine film to 64.6 ± 0.9 ns for $MA_{1-x}DMA_xPbI_3$ (x = 0.05) film was observed. This is attributed to the increase in crystalline quality and a reduction of defects as non-radiative recombination centres. With the presence of either spiro-MeOTAD (as hole extraction layer) or TiO_2 (as electron extraction layer), the

PL lifetimes drastically drop (Figure S5). Using the drift-diffusion model developed previously, the corresponding carrier diffusion coefficients and diffusion lengths were extracted [11]. We obtained an increased hole mobilty from 0.69 ± 0.09 $cm^2 s^{-1} V^{-1}$ at room temperature for $MAPbI_3$ film to 0.83 ± 0.06 $cm^2 s^{-1} V^{-1}$ for $MA_{1-x}DMA_xPbI_3$ (x = 0.05) film, yielding a hole diffusion length improvement from 280 ± 20 nm to 370 ± 20 nm. The electron mobility of $MA_{1-x}DMA_xPbI_3$ (x = 0.05) film slightly drops to 0.19 ± 0.02 $cm^2 s^{-1} V^{-1}$ from 0.29 ± 0.05 $cm^2 s^{-1} V^{-1}$ for $MAPbI_3$ film, yielding a comparable electron diffusion length of around 180 ± 20 nm in both cases due to a longer lifetime in the former (Table S3). We should also point out that the electron mobilities may be underestimated due to the presence of an injection barrier at the TiO_2/perovskite interface [41,42].

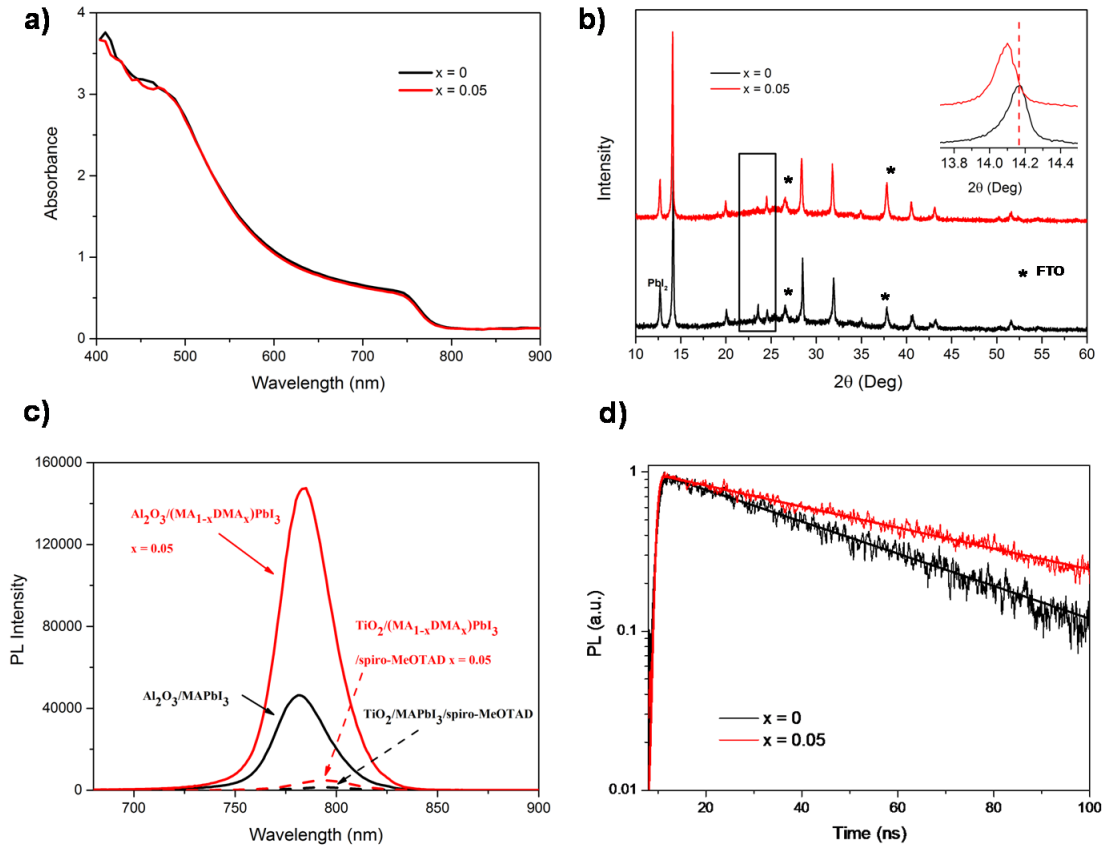

Fig. 3. (a) Absorption spectra, (b) X-ray diffraction spectra, (c) steady-state and (d) time-resolved photoluminescent spectra of the $MA_{1-x}DMA_xPbI_3$ (x = 0 and 0.05) films.

For device fabrication, the hole transporting material (HTM) was subsequently deposited by spin-coating a solution of spiro-MeOTAD, TBP, LiTFSI, and cobalt dopant (FK209) in chlorobenzene on to the prepared FTO/TiO_2/perovskite film. Finally, Au was evaporated as the back contact. Fig. 4a shows the current-voltage characteristics of the solar cells based on $MA_{1-x}DMA_xPbI_3$ (x = 0, 0.025, 0.05, 0.075, and 0.10), with the main parameters summarized in Table S4. The device based on $MAPbI_3$ (x = 0) displayed a short circuit photocurrent density (J_{sc}) of 19.61 mA cm^{-2}, an open circuit voltage (V_{oc}) of 1.09 V, and a fill factor (FF) of 0.76, resulting in a PCE of 17.1% under standard AM1.5G illumination. As DMA^+ was added, the best PCE of 18.6% was obtained at x = 0.05, with a dramatically improvement of J_{sc} from

19.61 mA cm^{-2} to 21.09 mA cm^{-2}. The higher J_{sc} was also validated by the incident photon-to-current conversion efficiency (IPCE) spectra. As shown in Fig. 4b, the photocurrent generation starts at around 800 nm in both cases, while the use of $MA_{1-x}DMA_xPbI_3$ (x = 0.05) gives a noticeable improvement of the photocurrent over the whole region either due to stronger light harvesting or more effective charge extraction. The IPCE is defined by the product of light harvesting efficiency (LHE), charge injection efficiency and charge collection efficiency. To find out the reason for the higher current, the LHE spectra were determined for $MA_{1-x}DMA_xPbI_3$ (x = 0 and 0.05). The LHEs are identical up to 550 nm, and then slightly lower with the presence of $MA_{1-x}DMA_xPbI_3$ (x = 0.05) comparing to that of $MAPbI_3$ (Fig. S6). As a result, the higher IPCEs and photocurrent for the solar cell based on $MA_{1-x}DMA_xPbI_3$ (x = 0.05) is mainly due to the more efficient charge extraction. $MAPbI_3$ has been reported to show a large built-in polarization due to the absence of inversion center with the presence of asymmetric organic cation [43]. In the cubic phase, the noncentrosymmetric organic cation must be orientationally disordered to satisfy the O_h symmetry, which has indirect effect on the intrinsic ferroelectricity by distorting the inorganic lattice [44]. Walsh et al. reported a large degree of polarization induced by the polar deformation of $[PbI_6]$ cage with the presence of a larger organic cation FA^+ [43]. In a similar way, the cubic $MA_{1-x}DMA_xPbI_3$ (x = 0.05) is expected to show a stronger polarization, which might have a potential advantage for efficient charge extraction.

Fig. 4c shows the *J-V* curves measured via the reverse and forward scans. There is almost no hysteresis for $MA_{1-x}DMA_xPbI_3$ (x = 0.05), indicating the stabilized crystal structure of $MA_{1-x}DMA_xPbI_3$ (x = 0.05). Under the same condition, the forward scan of the device with $MAPbI_3$ shows lower V_{oc} and FF, which eventually leads to around

1% lower efficiency (Table 2). Fig. S7 provide the statistical data on the reproducibility of the solar cell performance. The average PCEs based on $MAPbI_3$ and $MA_{1-x}DMA_xPbI_3$ (x = 0.05) calculated from 25 devices are 16.6±0.52% and 17.8±0.41%, respectively. The small deviation suggests good reproducibility. As mentioned before, partial replacement of MA^+ with bigger organic cation DMA^+ could construct a rigid [PbI_6] octahedral cage which is expected to show a better intrinsic thermal stability. To check this effect on the thermal stability of the materials, the unsealed solar cells based on $MA_{1-x}DMA_xPbI_3$ (x = 0 and 0.05) were kept in an ambient atmosphere (humidity > 50%) at 85°C, and the *J-V* curves were measured every 24 h. As shown in Fig. 4d, the PCE of the device based on $MA_{1-x}DMA_xPbI_3$ (x = 0.05) drops gradually from 18% to 13.4% after 7 days, mainly due to the decrease of J_{sc}. Under the same condition, the one with $MAPbI_3$ shows much faster degradation, with just 35% of its initial value left. This decay behavior is in good agreement with our previously speculation considering about the crystal configuration.

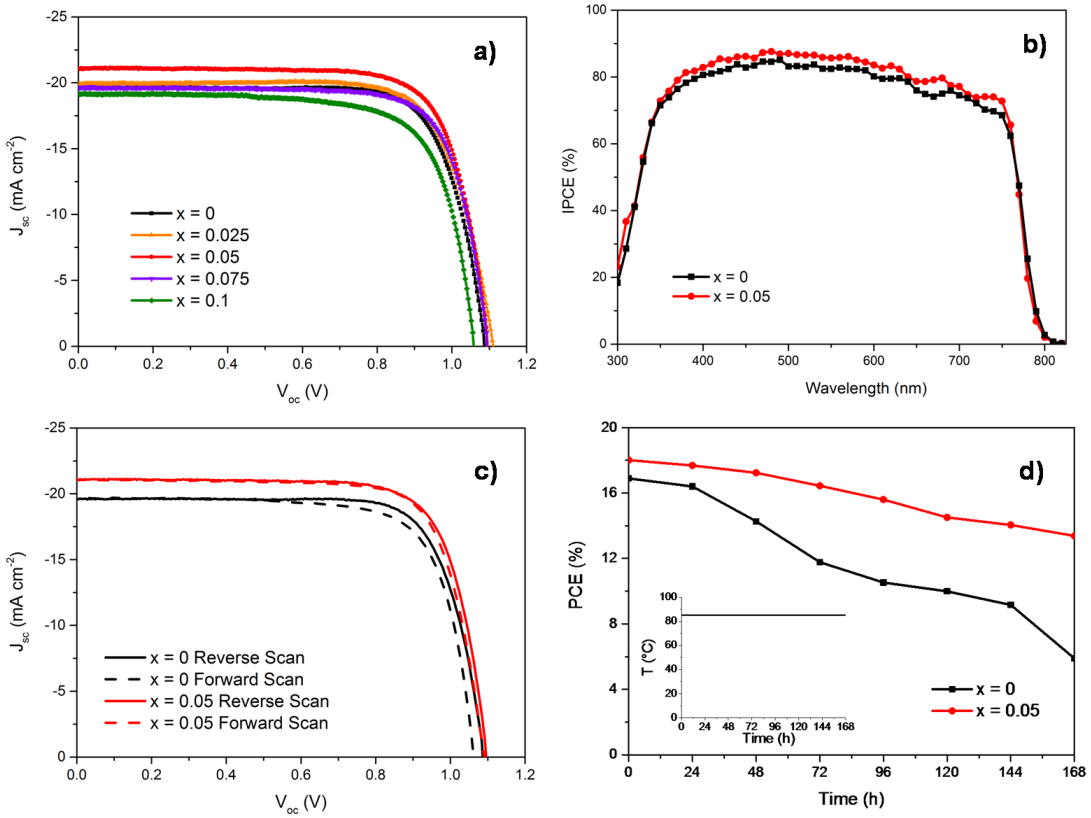

Fig. 4. (a) Current density-voltage (*J*-*V*) curves of $MA_{1-x}DMA_xPbI_3$ (x = 0, 0.025, 0.05, 0.075, and 0.10) solar cells measured under 95 mW cm^{-2} photon flux (AM 1.5 G). (b) The IPCE, (c) *J*-*V* hysteresis spectra of the devices, and (d) Degradation of PCE for the unencapsulated devices based on $MA_{1-x}DMA_xPbI_3$ (x = 0 and 0.05) keeping at 85°C under the ambient condition.

Table 2

Photovoltaic performance of the devices based on $MA_{1-x}DMA_xPbI_3$ under AM1.5G illumination (95 mW cm^{-2}).

		J_{sc} (mA cm^{-2})	V_{oc} (V)	FF	PCE (%)
x = 0	Reverse Scan	19.61	1.09	0.76	17.1
	Forward Scan	19.65	1.06	0.74	16.2
x = 0.05	Reverse Scan	21.09	1.10	0.76	18.6
	Forward Scan	21.08	1.09	0.76	18.4

4. Conclusion

In conclusion, we have investigated the organic cation effect by incorporating different amount of larger organic cation DMA^+ on the crystal lattice of $MAPbI_3$. The high-quality single crystals of $MA_{1-x}DMA_xPbI_3$ (x = 0 to 0.25) were prepared. By incorporating more than 6% of DMA^+, the formation of a stable cubic phase was obtained at room temperature. $MA_{0.91}DMA_{0.09}PbI_3$ crystallizes from a precursor solution with the MA^+/DMA^+ ratio of 0.95/0.05 and shows a *P*-43*m* space group and a cubic to tetragonal phase transition at 0°C. It exhibits the same band gap but more efficient charge extraction at the perovskite/charge transporting material interface comparing with that of $MAPbI_3$, leading to an improvement in device efficiency together with an enhanced thermal stability at 85°C. This study opens a way for the construction of intrinsically thermal-stable hybrid perovskites through the improvement the crystal symmetry.

Acknowledgements

The authors acknowledge the financial support from CAS pioneer Hundred talents program, Natural Science Foundation of Shanghai (17ZR1434400), National Key R&D Program of China (Grant No. 2016YFB 0901600), National Natural Science Foundation of China (Grants 61376056), Science and Technology Commission of Shanghai (Grant 16JC1401700), the Key Research Program of the CAS (Grants QYZDJ-SSW-JSC013). We thank Prof. Hui Zhang (Shanghai Institute of Microsystem and Information Technology) for the help of single crystal analysis. T. C. S acknowledges the financial support from the Ministry of Education Academic Research Fund Tier 1 grant RG173/16, and Tier 2 grants MOE2014-T2-1-044, MOE2015-T2-2-015 and MOE2016-T2-1-034; and from the Singapore National

Research Foundation through the NRF Investigatorship Programme NRF-NRFI-2018-04.

Appendix A. Supporting information

Appendix B. CCDC 1572441 contains the supplementary crystallographic data for this paper. These data can be obtained free of charge from The Cambridge Crystallographic Data Centre via www.ccdc.cam.ac.uk/data_request/cif.

Supplementary data associated with this article can be found in the online version.

References

[1] P. Gao, M. Grätzel, M. K. Nazeeruddin, Energy Environ. Sci. 7 (2014) 2448-2463.

[2] M. A. Green, A. Ho-Baillie, H. J. Snaith, Nat. Photon. 8 (2014) 506-514.

[3] S. Shi , Y. Li , X. Li , H. Wang, Mater. Horiz. 2 (2015) 378-405.

[4] J-W. Xiao, L. Liu, D. Zhang, N. D. Marco, J-W. Lee, O. Lin, Q. Chen, Y. Yang, Adv. Energy Mater. (2017), 1700491.

[5] A. B. Wong, M. Lai, S. W. Eaton, Y. Yu, E. Lin, L. Dou, A. Fu, P. Yang, Nano Lett. 15 (2015) 5519-5524.

[6] S. A. Veldhuis, P. P. Boix, N. Yantara, M. Li, T. C. Sum, N. Mathews, S. G. Mhaisalkar, Adv. Mater. 28 (2016) 6804-6834.

[7] X. Hu, X. Zhang, L. Liang, J. Bao, S. Li, W. Yang, Y. Xie, Adv. Funct. Mater. 24 (2014) 7373-7380.

[8] R. Dong, Y. Fang, J. Chae, J. Dai, Z. Xiao, Q. Dong, Y. Yuan, A. Centrone, X. C. Zeng, J. Huang, Adv. Mater. 27 (2015) 1912-1918.

[9] L. Etgar, P. Gao, Z. Xue, Q. Peng, A. K. Chandiran, B. Liu, M. K. Nazeeruddin, M. Grätzel, J. Am. Chem Soc. 134 (2012) 17396-17399.

[10] G. Giorgi, J-I. Fujisawa, H. Segawa, K. Yamashita, J. Phys. Chem. Lett. 4 (2013) 4213-4216.

[11] G. Xing, N. Mathews, S. Sun, S. S. Lim, Y. M. Lam, M. Grätzel, S. Mhaisalkar, T. C. Sum, Science 342 (2013) 344-347.

[12] Q. Dong, Y. Fang, Y. Shao, P. Mulligan, J. Qiu, L. Cao, J. Huang, Science 347 (2015) 967-970.

[13] W. J. Yin, T. Shi, Y. Yan, Adv. Mater. 26 (2014) 4653-4658.

[14] A. Kojima, K. Teshima, Y. Shirai, T. Miyasaka, J. Am. Chem. Soc. 131 (2009) 6050-6051.

[15] J-H. Im, C-R. Lee, J-W. Lee, S-W. Park, N-G. Park, Nanoscale 3 (2011) 4088-4093.

[16] H-S. Kim, C-R. Lee, J-H. Im, K-B. Lee, T. Moehl, A. Marchioro, S-J. Moon, R. Humphry-Baker, J-H. Yum, J. E. Moser, M. Grätzel, N-G. Park, Sci. Rep. 2 (2012) 591:1-7.

[17] J. Burschka, N. Pellet, S-J. Moon, R. Humphry-Baker, P. Gao, M. K. Nazeeruddin, M. Grätzel, Nature 499 (2013) 316-319.

[18] D. Liu, T. L. Kelly, Nat. Photon. 8 (2014) 133-138.

[19] J-H. Im, I-H. Jang, N. Pellet, M. Grätzel, N-G. Park, Nat. Nanotechnol. 9 (2014) 927-932.

[20] C. Roldan-Carmona, P. Gratia, I. Zimmermann, G. Grancini, P. Gao, M. Grätzel, M. K. Nazeeruddin, Energy Environ. Sci. 8 (2015) 3550-3556.

[21] Y. Zhang, P. Gao, E. Oveisi, Y. Lee, Q. Jeangros, G. Grancini, S. Paek, Y. Feng, M. K. Nazeeruddin, J. Am. Chem Soc. 138 (2016) 14380-14387.

[22] Y. Wu, F. Xie, H. Chen, X. Yang, H. Su, M. Cai, Z. Zhou, T. Noda, L. Han, Adv. Mater. 29 (2017) 1701073:1-8.

[23] S. S. Shin, E. J. Yeom, W. S. Yang, S. Hur, M. G. Kim, J. Im, K. Seo, J. H. Noh, S. I. Seok, Science 356 (2017) 167-171.

[24] W. S. Yang, B.-W. Park, E. H. Jung, N. J. Jeon, Y. C. Kim, D. U. Lee, S. S. Shin, J. Seo, E. K. Kim, J. H. Noh, S. I. Seok, Science 356 (2017) 1376-1379.

[25] M. A. Green, Y. Hishikawa, W. Warta, E. D. Dunlop, D. H. Levi, J. Hohl-Ebinger, A. W. Y. Ho-Baillie, Prog Photovolt Res Appl. 25 (2017) 668-676.

[26] N. H. Tiep, Z. Ku, H. J. Fan, Adv. Energy Mater. 6 (2016) 1501420.

[27] Z. Wang, Z. Shi, T. Li, Y. Chen, W. Huang, Angew. Chem. Int. Ed. 56 (2017) 1190-1212.

[28] A. D. Jodlowski, C. Roldan-Carmona, G. Grancini, M. Salado, M. Ralaiarisoa, S. Ahmad, N. Koch, L. Camacho, G. D. Miguel, M. K. Nazeeruddin, Nat Energy. 2 (2017) 972-979.

[29] M. Saliba, T. Matsui, K. Domanski, J.-Y. Seo, A. Ummadisingu, S. M. Zakeeruddin, J.-P. Correa-Baena, W. R. Tress, A. Abate, A. Hagfeldt, M. Grätzel, Science 354 (2016) 206-209.

[30] N. J. Jeon, J. H. Noh, W. S. Yang, Y. C. Kim, S. Ryu, J. Seo, S. I. Seok, Nature 517 (2015) 476-480.

[31] T. Baikie, Y. Fang, J. M. Kadro, M. Schreyer, F. Wei, S. G. Mhaisalkar, M. Grätzel, T. J. White, J. Mater. Chem. A 1 (2013) 5628-5641.

[32] C. C. Stoumpos, C. D. Malliakas, M. G. Kanatzidis, Inorg. Chem. 52 (2013) 9019-9038.

[33] H. Tsai, R. Asadpour, J.-C. Blancon, C. C. Stoumpos, O. Durand, J. W. Strzalka, B. Chen, R.Verduzco, P. M. Ajayan, S. Tretiak, J. Even, M. A. Alam, M. G. Kanatzidis, W. Nie, A. D. Mohite, Science 360 (2018) 67-70.

[34] Y. Zhang, G. Grancini, Y. Feng, A. M. Asiri, M. K. Nazeeruddin, ACS Energy Lett. 2 (2017) 802-806.

[35] W. Peng, X. Miao, V. Adinolfi, E. Alarousu, O. E. Tall, A-H. Emwas, C. Zhao, G. Walters, J. Liu, O. Ouellette, J. Pan, B. Murali, E. H. Sargent, O. F. Mohammed, O. M. Bakr, Angew. Chem. Int. Ed. 55 (2016) 10686-10690.

[36] Z. Shi, Y. Zhang, C. Cui, B. Li, W. Zhou, Z. Ning, Q. Mi, Adv. Mater. 29 (2017) 1701656: 1-6.

[37] Y. Liu, Z. Yang, D. Cui, X. Ren, J. Sun, X. Liu, J. Zhang, Q. Wei, H. Fan, F. Yu, X. Zhang, C. Zhao, S. Liu, Adv. Mater. 27 (2015) 5176-5183.

[38] W. Kong, Z. Ye, Z. Qi, B. Zhang, M. Wang, A. Rahimi-Iman, H. Wu, Phys. Chem. Chem. Phys. 17 (2015) 16405-16411.

[39] C. Roldan-Carmona, P. Gratia, I. Zimmermann, G. Grancini, P. Gao, M. Graetzel, M. K. Nazeeruddin, Energy Environ. Sci. 8 (2015) 3550-3556.

[40] Y. Zhang, P. Gao, E. Oveisi, Y. Lee, Q. Jeangros, G. Grancini, S. Paek, Y. Feng, M. K. Nazeeruddin, J. Am. Chem. Soc. 138 (2016) 14380-14387.

[41] G. Xing, B. Wu, S. Chen, J. Chua, N, Yantara, S. Mhaisalkar, N. Mathews, T. C. Sum, Small 11 (2015) 3606-3613.

[42] B. Wu, K. Fu, N. Yantara, G. Xing, S. Sun, T. C. Sum, N. Mathews, 5 (2015) 1500829.

[43] J. M. Frost, K. T. Butler, F. Brivio, C. H. Hendon, M. V. Schilfgaarde, A. Walsh, Nano Lett. 14 (2014) 2584-2590.

[44] W-L. Yan, G-H. Lu, F. Liu, J. Phys. Chem. C 120 (2016) 17972-17977.